SCIENCE CHINA

•Article•

https://doi.org/10.1007/s11431-022-2335-8

A strategy based on water soluble coal tar pitches to construct MnO_2@C composite materials with high electrochemical performance

LIU Bo[1], WANG Kun[1,4*], GUO ZhaoQi[1], HAN BeiBei[2,6], XU GuiYing[1*], JU DongYing[2,5], AN BaiGang[1], LI YongCheng[3], NI ZhenYong[3] & ZHOU WeiMin[1*]

1

2

3

4

5

6

Received November 16, 2022; accepted February 6, 2023; published online December 13, 2023

The water soluble coal tar pitches (WS-CTPs) were successfully prepared and used to construct the MnO_2@C composite materials by a hydrothermal method. It is interestingly observed that the structures and morphologies of MnO_2@C materials can be controlled by controlling the dosages of WS-CTPs and $KMnO_4$. Meanwhile, it is aware that MnO_2 exists in the MnO_2@C materials in an amorphous state. Compared with MnO_2, MnO_2@C materials output a remarkable improvement in electrochemical performance. For instance, MnO_2@C-0.3 shows the storage capacity at 965.7 mA h g^{-1} after 300 cycles at a current density of 0.1 A g^{-1}. In addition, after 600 cycles at a current density of 1.0 A g^{-1}, the storage capacity of MnO_2@C-0.3 still keeps 450.3 mA h g^{-1}, indicating that MnO_2@C-0.3 owns tremendous cycle stability at a high current density. In view of the fact that the coal tar pitches possess great cost advantages, the strategy of using WS-CTPs as a carbon source to cover the metal oxides is a competitive way to expand the application of metal oxides in the fabrication of electrodes of LIBs.

water soluble coal tar pitches, MnO_2, composite materials, lithium ion batteries (LIBs), energy storage systems (ESSs), coal tar pitches

Citation: Liu B, Wang K, Guo Z Q, et al. A strategy based on water soluble coal tar pitches to construct MnO_2@C composite materials with high electrochemical performance. Sci China Tech Sci, 2023, 66, https://doi.org/10.1007/s11431-022-2335-8

1 Introduction

Nowadays, the green energy sources have received attention from numerous nations worldwide as a means of reducing carbon emissions. Accelerating the development of energy storage systems (ESSs) is quickly becoming an effective countermeasure to store the energies which are produced by solar and wind energies. Lithium-ion batteries (LIBs) are a better choice for developing the ESSs due to their high energy density and long cycle life. Nevertheless, the low storage capacity of graphites is not satisfactory for the growing

*Corresponding authors (email: ustl15542731203@163.com; xuguiying751107@163.com; aszhou15242870697@163.com)

demands to develop ESSs [1–3].

As an alternative, a lot of research groups embark on the studies of metal oxides because they have extremely high storage capacity [4–7]. Among them, MnO_2 has been given a lot of attention because they possess the advantages such as high theoretical capacity (1230 mA h g^{-1}) and abundant resources [8,9]. Zhang et al. [10] successfully prepared the nano MnO_2 with high crystallinity and revealed it shows the significantly high storage capacity (1095 mA h g^{-1}) at 0.1 A g^{-1}. However, the large volume change generated during the storage of Li^+ facilely causes the collapse of the crystal, which results in the reduction of the long cycle performance of MnO_2. Meanwhile, the poor conductivity of MnO_2 easily leads to the production of polarization, and further decreases its rate performance [11,12].

It is well known that covering the carbon materials on the surface of MnO_2 is an effective way to solve the aforementioned problems. This method not only provides a possible solution to restrict the lattice expansion problem, but also provides an excellent conductive network for metal oxides, improving storage capacity [13,14]. Up to now, platy of carbon sources such as graphene and carbon nanotubes are widely used to cover the metal oxides [15–17]. However, the complex fabrication process and extremely high fabrication costs restrict the actual applications of these carbon sources. Coal tar pitches based carbons are coming into view of researchers because they have the contents of polycyclic aromatic hydrocarbons (PAHs) so that the carbons prepared by coal tar pitches exhibit the significantly excellent conductivity and cost advantage [18,19]. Zeng et al. [14] used coal tar pitches as carbon sources and a template method to construct carbon substrates, the MnO_2/PGC composite materials were synthesized based on the fabricated carbon substrates and precipitation method. Wang et al. [4] fabricated the metal oxide/carbon composite materials by directly mixing the coal tar pitches with the metal oxides. Nevertheless, these methods can not completely address issues such as agglomeration among the metal oxide particles and control of the sizes of metal oxides.

To address the aforementioned problems, the water soluble coal tar pitches (WS-CTPs) were prepared and used as the covering materials. The WS-CTPs possess the characteristics of good water solubility and contain a lot of PAHs, causing that the WS-CTPs are able to become excellent carbon sources for fabricating the metal oxides/carbon composite materials. Thus, based on the usage of a hydrothermal method, the novel WS-CTPs based MnO_2@C materials were successfully synthesized by using the $KMnO_4$ and WS-CTPs. It is interestingly found that MnO_2 exists in the MnO_2@C materials in the amorphous state, and the MnO_2@C composite materials manifest different structures with conversing the dosages of WS-CTPs.

After detailed electrochemical investigations, it is observed that the MnO_2@C materials exhibit the fabulous storage capacity. It is noteworthy that a lot of defects on amorphous MnO_2 provided the active sites for storing Li^+, leading to the enhancement of storage capacity. Considering the fact that coal tar pitches are industrial commodities, the WS-CTPs based MnO_2@C materials exhibit significant cost advantages in the fabrication of EES.

2 Experimental

2.1 Characterization

The AVATAR 360 infrared spectrometer (FT-IR) was used to analyze the functional groups on the surfaces of the samples. The X-ray diffraction (XRD) patterns were measured with an X'pert Powder instrument from PANalytical at 40.0 kV and 40 mA with Cu-Kα radiation. The results of X-ray photoelectron spectroscopy (XPS) were verified by a K-Alpha instrument using an Al-Kα source (12 kV) from Thermo Fisher Scientific, USA. The structures of the samples were analyzed by the HR 800 laser Raman spectrometer of Horiba Jobin Yvon company, France. Nitrogen adsorption and desorption isotherms were measured by a Quadrasorb autosorb-iQ surface analyzer which was purchased from Quantachrome Instruments, USA. The specific surface area was evaluated, according to the Brunauer-Emmett-Teller (BET) method. Based on a DFT model the size distributions were evaluated. Morphological features were described by scanning electron microscopy (SEM) using an instrument produced by Carl Zeiss AG, Germany. TEM measurements were performed on the HF-3300 system (Hitachi Co. Ltd., Tokyo, Japan). Thermogravimetry (TG) measurements were recorded using a Rigaku TG-DTA8122 thermal analyzer under a flow of air with a heating rate of 10°C/min. Cyclic voltammetry (CV) and electrochemical impedance spectroscopy (over a frequency range of 100 kHz–0.01 Hz and the amplitude was 5 mV) were tested by CHI660E electrochemical workstation (ChenHua, Shanghai, China).

2.2 Preparations of water soluble coal tar pitch based carbons (WS-CTPCs)

The coal tar pitch (5 g) was added in a mortar and ground in size which is less than 45 μm. Then, the sulfuric acid (95 wt%–98 wt%, 70 mL) and nitric acid (65 wt%–68 wt%, 30 mL) were added to a round-bottom flask, and then this acid mixture was stirred for 5 h at 40°C. After the reaction, the mixture was filtered, and the obtained solids were washed by de-ionized water until the pH value of washed solution became neutral. The obtained solids were mixed with NaOH (1 mol L^{-1}) until the pH value of the obtained mixture was over 12, and then this mixture was continuously stirred for 1 h at 80°C. Thereafter, the HCl (1 mol L^{-1}) was added to the

same mixture until its pH value was smaller than 2. At the same time, it was observed that black solids formed in this mixture. The solids were obtained by centrifugal separation and then placed in a drying oven for 12 h at 80°C. Finally, the obtained solids were named as water soluble coal tar pitches (WS-CTPs), and placed in a tube furnace for 5 h at 400°C in N_2 atmosphere. The obtained carbons that are processed with carbonization were named WS-CTPCs.

2.3 Preparation of CTPs based MnO_2@C composite materials

The $KMnO_4$ (0.5 g), H_2SO_4 (0.3 mL) and deionized water (15 mL) were mixed, and then this mixture was named as solution. WS-CTPs were dissolved in the deionized water (20 mL), and the 1 mol L^{-1} NaOH was dropped into the solutions containing WS-CTPs until its pH value became 10. The solution containing WS-CTPs was named solution. The solution was mixed with solution, and then the obtained mixture was stirred uniformly. This mixture was placed in a high-pressure reactor for 6 h at 150°C. After cooling down to the room temperature, this mixture was filtered, and the obtained solids were placed in a drying oven for 12 h at 80°C. Finally, the obtained solids were placed in a tube furnace for 5 h at 400°C in N_2 atmosphere. According to the adding amount of WS-CTPs (0.3, 0.4 and 0.5 g), the obtained MnO_2@C composite materials were named as MnO_2@C–X (X = 0.3, 0.4 and 0.5), respectively. Nevertheless, the solids did not form when a dosage of WS-CTPs was set at 0.2 g.

2.4 Electrochemical measurements

The electrochemical cells were assembled by using the MnO_2@C composite materials. The MnO_2@C composite materials (0.08 g) were respectively mixed with acetylene black (0.015 g) and polyvinylidine fluoride (PVDF) binder (0.005 g) in a weight ratio of 80:15:5 in -methyl-2-pyrrolidone (NMP) solution. The fabricated slurry was coated on the Cu foil and dried in a vacuum drying oven at 80°C for 1 h so as to remove the solution. Continuously, the Cu foil with the active materials was dried at 120°C for 12 h, and cut into round shape strips of 11 mm. The mass loading of the active materials was at 1.20 mg/cm^2. The two-electrode electrochemical cells (CR2032 coin-type) were assembled in a glove box filled with high-purity argon. The lithium metal foil (15.60 mm × 0.45 mm) was a reference electrode. Celgard 2400 micro-porous membrane was a separator, and 1 mol L^{-1} $LiPF_6$ in the mixture of EC, DMC, EMC (1:1:1, vol%) was an electrolyte. Galvanostatic charge-discharge tests were conducted by LAND (CT 2001A) battery test system at a 0.01–3.00 V. CV and electrochemical impedance spectroscopy (EIS) measurements were performed by using the CHI 660E. The CV curves were recorded in a voltage region of 0.01–3.00 V at a scan rate of 0.2 mV/s. The impedance spectra were recorded in a frequency range of 100 kHz–0.01 Hz.

3 Results and discussion

The synthesis procedures of MnO_2@C-0.3 material are described in Figure 1. The carbon contents in MnO_2@C materials were first determined by TGA measurements (Figure S1). The slight mass loss occurring below 200°C is generally attributed to the loss of water. The significant weight losses were observed at a temperature range of 350°C–500°C, which was ascribed to the burning of carbons of MnO_2@C materials. When the temperature was increased to 550°C, the weight loss became negligible [20,21]. After calculations, the carbon contents of MnO_2@C-0.3, MnO_2@C-0.4 and MnO_2@C-0.5 were 34%, 45%, and 53%, respectively.

In the comparison with the CTPs, the conversions of groups on WS-CTPs were verified by FT-IR measurements. It was distinct that novel peaks of 1045, 1345, 1530 and 1720 cm^{-1} corresponding to the –C–O, –C–OH, $–NO_2$ and –C=O groups appeared in the WS-CTPs (Figure S2(a)) [22–24]. Meanwhile, the intensity of 3420 cm^{-1} attributing to

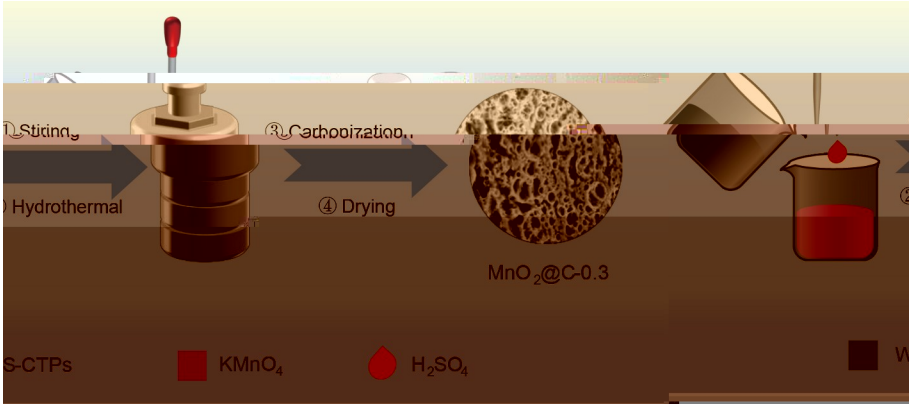

Figure 1 (Color online) Synthesis procedures of MnO_2@C-0.3 material.

the –OH group increased in the WS-CTPs. The existences of hydrophilic functional groups cause that WS-CTPs are able to dissolve in water (Figure S2(b)). Zhang et al. [25] indicated that the oxygen functional groups on the surface of carbon materials can help to increase the dispersion ability of carbon materials and the adsorption ability for metal ions, leading to the excellent dispersion of nano-sized metal oxide. Likewise, it is also considerable that nano MnO_2 can be dispersed in carbon substrates very well.

To inquire into the chemical states of MnO_2@C materials, the XPS measurements were performed in detail. As shown in Figure 2(a), the binding energies of Mn $2p_{1/2}$ and Mn $2p_{3/2}$ were observed at 653.0 and 641.2 eV, respectively. Especially, the differences between the binding energies are 11.8 eV, which corresponds to a feature of MnO_2 [26]. After fitting the two peaks of Mn $2p_{1/2}$ and Mn $2p_{3/2}$, the mixed oxidation states of Mn^{4+} and Mn^{3+} were observed at 655.0, 643.4 eV (Mn^{4+}) and 653.2, 641.4 eV (Mn^{3+}), respectively [27]. At the present stage, the existence of Mn^{3+} demonstrates the abundant structural defects nature, which probably plays a role to facilitate the formation of the amorphous state [28,29]. The peak of N 1s was able to be fitted to the ~398.5 eV (N-6) and ~400.0 eV (N-5), respectively, indicating that N elements of WS-CTPs exist in MnO

that carbons in MnO_2@C are in the amorphous state [24,33]. Compared with the MnO_2, the characteristic peak of Mn–O (648.9 cm^{-1}) slightly shifted to the right and then became broad in the MnO_2@C materials, which suggests that the MnO_2 of the MnO_2@C materials is in the amorphous state [34,35].

In the TEM image, the long-range ordered structures were not observed in the MnO_2@C materials, which was indicative that the MnO_2 and carbons in the MnO_2@C materials exist in an amorphous state. The corresponding fast Fourier transform (FFT) image can further confirm the amorphous nature of MnO_2@C materials (Figure 3(c)). Additionally, it was different from the characteristic interlamellar spacing (0.363 nm) of carbons, an observation of lattice fringes with an interplane distance of 0.690 nm is probably attributed to the MnO_2 [17,29,36]. These aforementioned XPS, XRD, Raman and TEM measurements furnish convincing proof that MnO_2 compounds exist in the MnO_2@C composite materials as an amorphous state.

The morphologies of MnO_2 and MnO_2@C materials were described in (Figure 4(a)–(c)). Firstly, the synthesized MnO_2 is constructed by the nano-sized fibers with a witch of ~48 nm, as shown in Figure S4. By contrast, it is obvious that the morphologies of MnO_2 exceedingly changed in MnO_2@C materials (Figure 4(a)–(c)). One possible explanation for this may be the hydrophilic functional groups in WS-CTPs break the formation of MnO_2 crystals. It is noteworthy that MnO_2@C-0.3 shows the well-developed and cross-linked pore structures, which facilely facilitate the infiltration of electrolyte to improve the charge transfer [37,38]. Additionally, SEM-EDX mapping indicates that C, O, Mn and N elements dispersed homogeneously (Figure S5). With increasing the dosages of WS-CTPs, it was observed that a lot of spherical particles fused to each other, leading to the formations of rodlike structures in MnO_2@C-0.4 material. Furthermore, the MnO_2@C-0.5 approximately was the uneven block structure, which implies the poor dispersion between each component of metal oxide@C composites. The noticeable conversions of morphologies are likely caused to the increase of hydrogen bonds between the –COOH and –OH groups of WS-CTPs in reactive cases, with increasing the addition amount of WS-CTPs. These hydrogen bond interactions among the coal tar pitches can decrease the thermal decompositions of coal tar pitches, decreasing the formation of complex porous structures. Meanwhile, the hydrogen bond interactions also decrease the dispersion of MnO_2 in MnO_2@C materials, which is able to decrease the formations of complex porous structures [39].

The nitrogen adsorption experiment was performed to examine the pore characteristics of MnO_2@C materials (Figure S6). After calculations, the specific surface areas of MnO_2, MnO_2@C-0.3, MnO_2@C-0.4 and MnO_2@C-0.5 were 45.2, 84.7, 362.4 and 290.7 $m^2\ g^{-1}$, respectively (Table S1). Compared with the MnO_2@C-0.4 and MnO_2@C-0.5, the MnO_2@C-0.3 owned extremely complex porous structures (Figure 4(d)). In particular, the existences of numerous mesoporous in MnO_2@C-0.3 are able to provide a tremendous transmission channel for Li^+ ions, causing the chemical kinetics of MnO_2@C-0.3 to increase remarkably [40–43].

On the basis of evaluations for structures of MnO_2@C materials, their electrochemical performance was synthetically investigated. In the cycling performance, the MnO_2 only showed the storage capacity at 60 mA h g^{-1} after 100 cycles. By contrary, the MnO_2@C-0.3, MnO_2@C-0.4 and

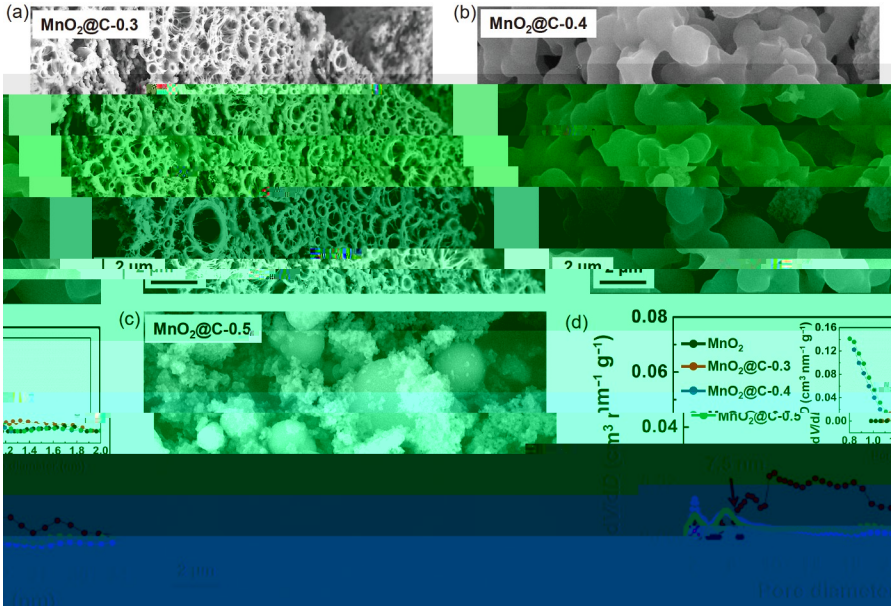

Figure 4 (Color online) (a)–(c) SEM morphologies of MnO_2@C materials; (d) pore size distribution curves of MnO_2 and MnO_2@C materials.

MnO_2@C-0.5 exhibited the storage capacity at 865.2, 647.2 and 420.9 mA h g^{-1} after 100 cycles, respectively. These results indicate that covering carbon materials on the surface of MnO_2 is an efficacious way to enhance the actual storage capacity of MnO_2 (Figure 5(a)). Meanwhile, the formation of MnO_2 in the amorphous state is also beneficial to prevent the breaking of structures in the repeated Li insertion-extraction process, enhancing the storage capacity and cycling stability [44–46]. Similar to the general metal oxides such as MnO , Fe_2O_3 and Co_3O_4, the trend from decline to rise in cycling performance is also obviously observed in MnO_2@C-0.3. Likewise, with the proceeding of the charge-discharge process, the breaking of SEI and then forming of a polymeric gel-like film cause an appearance of the above-mentioned phenomenon in the cycling performance of MnO_2@C-0.3 [30,47,48].

As shown in Figure 5(b), the MnO_2@C-0.3 manifested more tremendous rate performance than others. For instance, when the current densities were set at 0.1, 0.2, 0.5, 1.0, 2.0 and 5.0 A g^{-1}, the storage capacity of MnO_2@C-0.3 was 734.1, 586.8, 516.8, 428.2, 318.9 and 129.5 mA h g^{-1}, respectively. As shown in Figure 5(c)–(d), the long cycling stability of MnO_2@C-0.3 was also investigated. Surprisingly, after the initial decrease, the discharge capacity of MnO_2@C-0.3 gradually increases to 965.7 mA h g^{-1} at 0.1 A g^{-1} after 300 cycles. Furthermore, MnO_2@C-0.3 still possesses an excellent capacity of 450.3 mA h g^{-1} after 600 cycles, even at a higher current density of 1.0 A g^{-1}. As far as reversible capacity and rate performance are concerned, it is clear that the MnO_2@C-0.3 presents superior lithium storage performance compared with some previously reported manganese oxides (Table S2).

CV curves of MnO_2 and MnO_2@C materials were illustrated in Figures S7(a) and 6(a)–(c). As shown in Figure S7(a), two reductive peaks were observed at 1.8 and 1.0 V in the first cycle, respectively, which correspond to the reduction Mn^{4+} to Mn^{2+} ($MnO_2+2Li^++2e^- \rightarrow MnO+Li_2O$) and the further reduction from Mn^{2+} to Mn^0 ($MnO+2Li^++2e^- \rightarrow Mn+Li_2O$), respectively [10]. The reductive peak at 0.1 V in the first cycle was generally attributed to the formation of solid electrolyte interphase (SEI) and side reactions between Li^+ and active materials. In addition, the oxidative peak at 1.1 V was considered a result of a reaction of Mn^0 to Mn^{2+} [14,16]. However, these reductive and oxidative peaks were rarely observed from the second cycle, which is possibly due to the breaking structures of MnO_2.

On the basis of analyses of MnO_2, the electrochemical characteristics of MnO_2@C-0.3 were performed in detail. The two reductive peaks (0.7 and 1.4 V) appear at the second cycle of MnO_2@C-0.3, corresponding to a two-step possible reduction process $Mn^{3+/4+}$ to Mn^{2+}, Mn^{2+} to Mn^0 (Figure 6(a)). Two oxidative peaks located in 1.1 and 2.1 V could con-

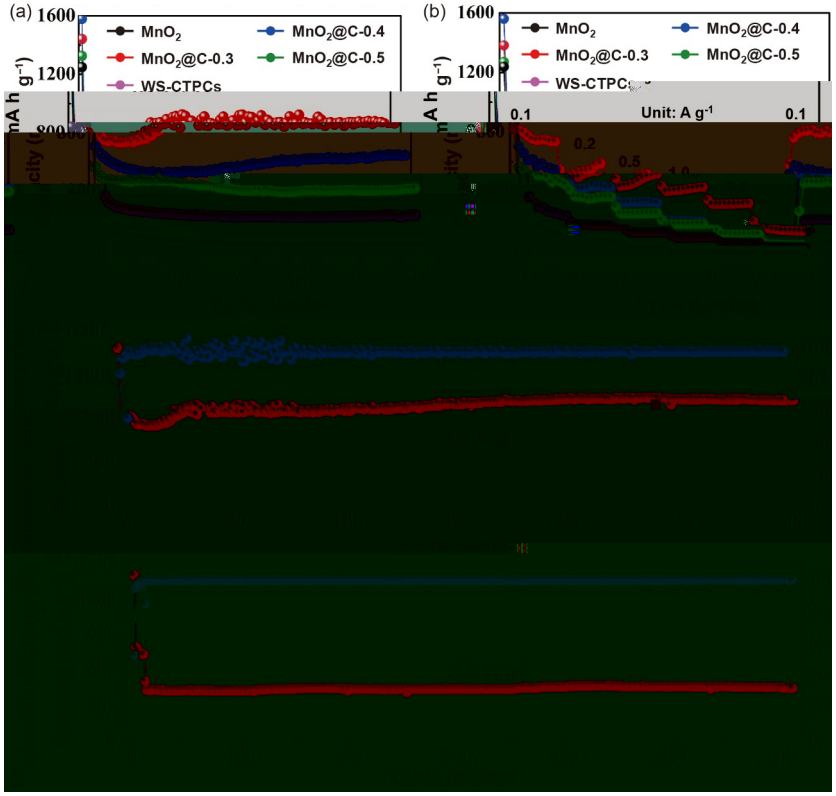

Figure 5 (Color online) (a) Cycling performance of WS-CTPCs, MnO_2 and MnO_2@C materials; (b) rate performance of WS-CTPCs, MnO_2 and MnO_2@C materials; (c) storage capacity of MnO_2@C-0.3 at 0.1 A g^{-1} after 300 cycles; (d) storage capacity of MnO_2@C-0.3 at 1.0 A g^{-1} after 600 cycles.

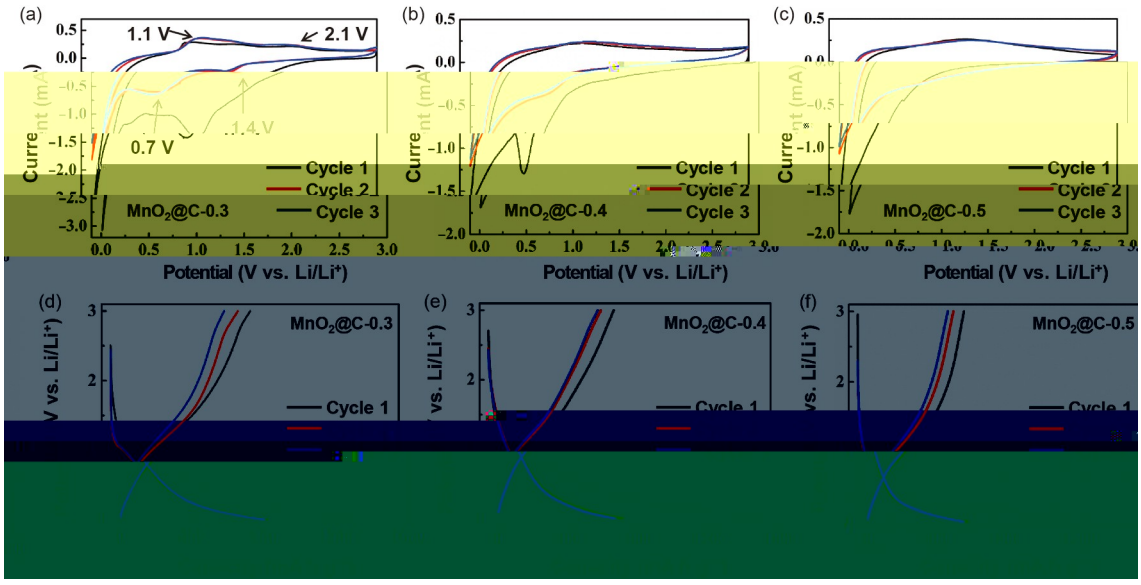

Figure 6 (Color online) (a)–(c) CV curves of MnO_2@C materials; (d)–(f) charge-discharge profiles of MnO_2@C materials.

ceivably be hypothesized that the reoxidation of manganese contains two steps, which demonstrates that the oxidation process of Mn to MnO_2 is a two-step reaction process [49]. Associated with the evaluative results of XRD, the slightly shifting left was probably attributed to that the MnO_2 of MnO_2@C-0.3 is in the amorphous state, leading to the conversions of CV measurement results of MnO_2 and MnO_2@C-0.3. In addition, it is different from the MnO_2 (Figure S7(a)), the four peaks still exist from the second cycle (Figure 6(a)), which is strongly suggestive that covering the carbon materials is the effective way to overcome the breaking of MnO_2 in the charge-discharge processes. However, the peaks were not observed obviously in the MnO_2@C-0.4 and MnO_2@C-0.5 materials, revealing the excess amount of WS-CTPs is not suitable for developing the electrochemical performance of MnO_2 (Figure 6(b)–(c)).

The electrochemical performance of MnO_2 and MnO_2@C materials were further verified by the charge-discharge measurements (Figure 6(d)–(f)). The first coulombic efficiencies of MnO_2@C-0.3, MnO_2@C-0.4 and MnO_2@C-0.5 were 56.2%, 45.5% and 47.3%, respectively. Generally, the low first coulombic efficiencies are attributed to the formation of SEI and irreversible reactions between Li^+ and active materials. Compared with the MnO_2 (Figure S7(b)), it was observed that MnO_2@C-0.3 exhibited a sloping charge-discharge plateau, which is probably ascribed to the enhancement of pseudocapacitance effect [50,51]. By contrast, this sloping plateau was not observed in the MnO_2@C-0.4 and MnO_2@C-0.5 materials. On the basis of the aforementioned analyses, it can be assumed that dimensional hierarchical porous structures of MnO_2@C-0.3 are conducive to enhance its pseudocapacitance effect [49,52].

The charge transfer abilities of MnO_2 and MnO_2@C materials were evaluated by electrochemical impedance spectroscopy (EIS) measurements (Figure 7). Figure 7(a) exhibited that MnO_2@C-0.3 possessed the smaller diameters of semicircle loop at high frequency region than MnO_2 and other MnO_2@C materials, suggesting that MnO_2@C-0.3 showed a more excellent conductivity than the others. Additionally, according to Yang et al. [7] and Tai et al. [9], the $_{ct}$ values of MnO_2@C-0.3, MnO_2@C-0.4 and MnO_2@C-0.5 were calculated at 56.12, 68.08 and 263.90 Ω, respectively, revealing the MnO_2@C-0.3 owned more tremendous charge transfer properties. It is considerable that three dimensional hierarchical porous structures and excellent dispersions of MnO_2 in MnO_2@C-0.3 accelerate the Li^+ transfer so that the reaction kinetics of MnO_2@C-0.3 were improved remarkably [53].

In general, the value of the Warburg coefficient is used to evaluate the Li diffusion performance. The Randles plot plotting of ′ with $^{-1/2}$ ($=2\pi$) for a low-frequency is used to obtain values (Figure 7(b)). Namely, the larger value reflects the poor ion diffusion performance [54]. As a result, the values of MnO_2@C-0.3, MnO_2@C-0.4 and MnO_2@C-0.5 were respectively calculated as 65.5, 72.2 and 209.2 Ω/s$^{1/2}$, indicating that the MnO_2@C-0.3 owned the exceedingly higher Li^+ diffusion performance than other MnO_2@C materials. The excellent transfer ability of MnO_2@C-0.3 was attributed to its complicated structures. Therefore, it is thought that adjusting the dosages of WS-CTPs is an effective way to synthesize the MnO_2@C composite materials having fabulous electrochemical performance.

In accordance with a report by Wang et al. [52], the storage

mechanism of MnO_2@C-0.3 was finally discussed. As shown in Figure 8(a), it was obviously found that the MnO_2@C-0.3 exhibited excellent electrochemical stability at different scan rates in a voltage range of (0.01–3.00 V). After detailed calculations, the fact that the capacitive effect occupied a relatively large proportion (64.0%) for a contribution of storing Li^+ was observed, which is higher than that of MnO_2@C-0.4 (60.7%) and MnO_2@C-0.5 (46.4%), respectively (Figure 8(d)–(f)). Because the specific surface area of MnO_2@C-0.3 is relatively small (84.7 m^2 g^{-1}), the main capacitive contribution could be considered as pseudocapacitance rather than double layer charging. In summary, the high pseudocapacitance contribution is ascribed to the rapid electron transfer. The existence of abundant structural defects in MnO_2 can reduce the energy barrier of charge transfer during the redox reaction, while the nitrogen and oxygen elements in the carbon contents serve as active sites to store lithium ions reversibly [53,55,56].

4 Conclusion

The WS-CTPs were prepared using coal tar pitches according to a mixing acid method. The MnO_2@C composite materials were successfully synthesized by using the $KMnO_4$ and WS-CTPs. It is observed that complex porous structures of MnO_2@C can be controlled by adjusting the addition amount of reactive materials of $KMnO_4$ and WS-CTPs. The complex porous structures and MnO_2 in the amorphous state enhanced the pseudocapacitance of MnO_2@C materials, leading to remarkable improvement in their storage capacity. As an example, the storage capacity MnO_2@C-0.3 is 965.7 mA h g^{-1} after 300 cycles at a current density of 0.1 A g^{-1}. When the current density was set at 1.0 A g^{-1}, the MnO_2@C-0.3 still exhibits the storage capacity at 450.3 mA h g^{-1} after 600 cycles. In light of the fact that the coal tar pitches possess the cost-effective advantage, we will consider that the method using WS-CTPs as a carbon source

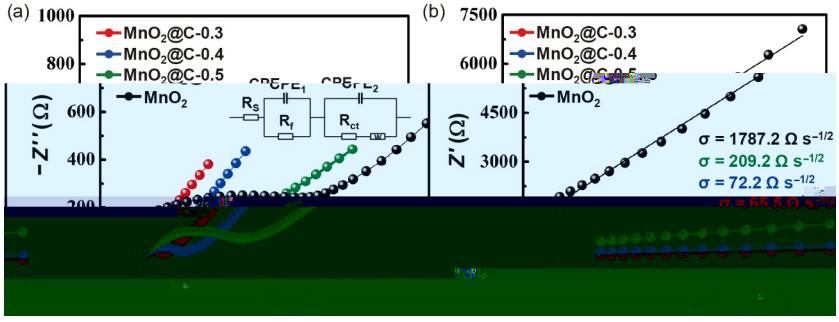

Figure 7 (Color online) Nyquist plot results (a) and illustrations of relationships between ′ and $^{-1/2}$ in the low-frequency region (b). Among them, $_s$ represents the resistances associated with solution, wires, and contacts. $_f$ and CPE_1 (constant phase element) represent the Faradaic and non-Faradaic pathways of the SEI layer, respectively. $_{ct}$ is the charge transfer resistance, together with another CPE_2, represents the charge transfer reaction. The Warburg element stands for the diffusion kinetics of the Li ion through the electrode materials.

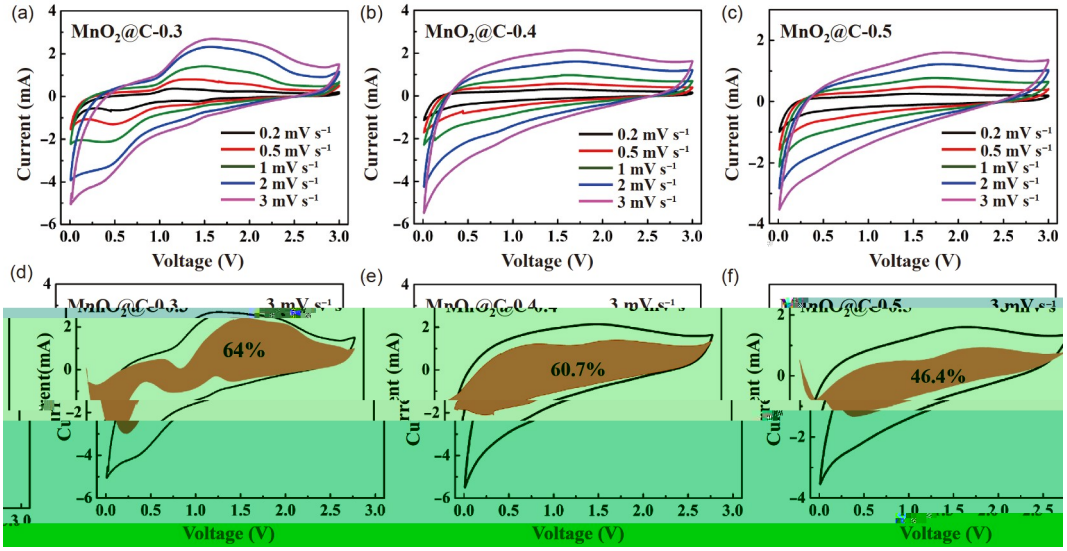

Figure 8 (Color online) (a)–(c) CV curves of MnO_2@C materials at different scan rates. (d)–(f) Capacitive contributions of MnO_2@C materials at a scan rate of 3 mV s^{-1}.

is a significantly favorable way to expand actual applications of metal oxides in fabrications of electrode materials of LIBs.

Supporting Information

The supporting information is available online at tech.scichina.com and link.springer.com. The supporting materials are published as submitted, without typesetting or editing. The responsibility for scientific accuracy and content remains entirely with the authors

1 Huang Y, Tang Y, Yuan W, et al. Challenges and recent progress in thermal management with heat pipes for lithium-ion power batteries in electric vehicles. Sci China Tech Sci, 2021, 64: 919–956
2 Li J, Xu G, Wang K, et al. Study on fabrication and electrochemical performances of Fe_7S_8@C composite materials. Electrochemistry, 2020, 88: 380–386
3 Wang K, Ju D, Xu G, et al. Enhanced Li ion storage performances of carbon black by introducing organosulfur groups on surface. Electrochemistry, 2020, 88: 8–13
4 Wang K, Ju D, Xu G, et al. Study on electrochemical performances of composite carbon (FeO/C) materials fabricated by coal tar pitch and Fe_3O_4 particles. Int J Hydrogen Energy, 2019, 44: 25199–25206
5 Wang L, Nie Z, Cao C, et al. Carbon-wrapped TiO_2 nanocubes exposed with (001) active facets for high-rate and long-life lithium-ion batteries. J Power Sources, 2016, 302: 259–265
6 Zhang J, Zhu Y, Cao C, et al. Microwave-assisted and large-scale synthesis of SnO_2/carbon-nanotube hybrids with high lithium storage capacity. RSC Adv, 2015, 5: 58568–58573
7 Yang L, Wu Y, Wu Y, et al. Hierarchical flower-like Fe_2O_3 mesoporous nanosheets with superior electrochemical lithium storage performance. J Energy Storage, 2019, 23: 363–370
8 Khalid S, Cao C, Naveed M, et al. 3D hierarchical MnO_2 microspheres: A prospective material for high performance supercapacitors and lithium-ion batteries. Sustain Energy Fuels, 2017, 1: 1795–1804
9 Tai Z, Shi M, Zhu W, et al. Carbon-coated β-MnO_2 for cathode of lithium-ion battery. Sustain Energy Fuels, 2020, 4: 1704–1711
10 Zhang L, Song J, Liu Y, et al. Tailoring nanostructured MnO_2 as anodes for lithium ion batteries with high reversible capacity and initial coulombic efficiency. J Power Sources, 2018, 379: 68–73
11 Meng Y, Liu Y, He J, et al. Large scale synthesis of manganese oxide/reduced graphene oxide composites as anode materials for long cycle lithium ion batteries. ACS Appl Energy Mater, 2021, 4: 5424–5433
12 Park J H, Choi W Y, Lee S, et al. Graphene intercalated free-standing carbon paper coated with MnO_2 for anode materials of lithium ion batteries. Electrochim Acta, 2020, 348: 136310
13 Zhang M, Jin D, Zhang L, et al. High energy storage MnO_2@C fabricated by ultrasonic-assisted stepwise electrodeposition and vapor carbon coating. Chem Eng J Adv, 2021, 6: 100098
14 Zeng H, Xing B, Zhang C, et al. synthesis of MnO_2/porous graphitic carbon composites as high-capacity anode materials for lithium-ion batteries. Energy Fuels, 2020, 34: 2480–2491
15 Abdollahi A, Abnavi A, Ghasemi F, et al. Facile synthesis and simulation of MnO_2 nanoflakes on vertically aligned carbon nanotubes, as a high-performance electrode for Li-ion battery and supercapacitor. Electrochim Acta, 2021, 390: 138826
16 Song J, Li Y, Tong R, et al. Mn O embedded within CNT supporting porous carbon for enhanced lithium storage. J Phys Chem Solids, 2022, 160: 110317
17 Wang Z, Yan X, Wang F, et al. Reduced graphene oxide thin layer induced lattice distortion in high crystalline MnO_2 nanowires for high-performance sodium- and potassium-ion batteries and capacitors. Carbon, 2021, 174: 556–566
18 Xing B, Zhang C, Liu Q, et al. Green synthesis of porous graphitic carbons from coal tar pitch templated by nano-$CaCO_3$ for high-performance lithium-ion batteries. J Alloys Compd, 2019, 795: 91–102
19 Li Y, Liu X, Liu L, et al. Coal tar electrode pitch modified rice husk ash as anode for lithium ion batteries. J Electrochem Soc, 2019, 166: A2425–A2430
20 Chen J, Yang K, Wang J, et al. Peanut-like yolk/core-shell MnO/C microspheres for improved lithium storage and the formation mechanism of $MnCO_3$ precursors. J Alloys Compd, 2020, 849: 156637
21 Park S K, Jin A, Yu S H, et al. hydrothermal synthesis of Mn_3O_4 nanoparticles on nitrogen-doped graphene as high-Performance anode materials for lithium ion batteries. Electrochim Acta, 2014, 120: 452–459
22 Bourlinos A B, Gournis D, Petridis D, et al. Graphite oxide: Chemical reduction to graphite and surface modification with primary aliphatic amines and amino acids. Langmuir, 2003, 19: 6050–6055
23 Szabó T, Berkesi O, Forgó P, et al. Evolution of surface functional groups in a series of progressively oxidized graphite oxides. Chem Mater, 2006, 18: 2740–2749
24 Wang K, Ju D Y, Xu G Y, et al. Organosilicon modified method to improve Li^+ storage capacity of graphene oxide (GO). Sci China Tech Sci, 2020, 63: 2709–2716
25 Zhang W, Xu H, Xie F, et al. General synthesis of ultrafine metal oxide/reduced graphene oxide nanocomposites for ultrahigh-flux nanofiltration membrane. Nat Commun, 2022, 13: 471–480
26 Jia H N, Lin J H, Liu Y L, et al. Nanosized core-shell structured graphene-MnO_2 nanosheet arrays as stable electrodes for superior supercapacitors. J Mater Chem A, 2017, 5: 10678–10686
27 Kim I G, Ghani F, Lee K, et al. Electrochemical performance of Mn_3O_4 nanorods by N-doped reduced graphene oxide using ultrasonic spray pyrolysis for lithium storage. Int J Energy Res, 2020, 44: 11171–11184
28 Ang Z W J, Xiong T, Lee W S V, et al. Oxygen-deficient birnessite-MnO_2 for high-performing recha eq ctra i u ha ra

M W

anodes for lithium and sodium ions batteries. J Alloys Compd, 2021, 863: 158078
38 Wei F, Zhang H, He X, et al. Synthesis of porous carbons from coal tar pitch for high-performance supercapacitors. New Carbon Mater, 2019, 34: 132–139
39 Luo J, Hu W, Suo Z, et al. Co-pyrolysis of spent radioactive ion exchange resin and manganese dioxide: Decrease the decomposition temperatures of functional groups. J Hazard Mater, 2021, 418: 126275
40 Zhong S, Zhang H, Fu J, et al. synthesis of 3D carbon coated zinc-cobalt bimetallic oxide networks as anode in lithium-ion batteries. ChemElectroChem, 2018, 5: 1708–1716
41 Vijayan B L, Misnon I I, Anil Kumar G M, et al. Facile fabrication of thin metal oxide films on porous carbon for high density charge storage. J Colloid Interface Sci, 2020, 562: 567–577
42 Moon S, Kim D H, Kwak J H, et al. Unveiling the pseudocapacitive effects of ultramesopores on nanoporous carbon. Appl Surf Sci, 2021, 537: 148037
43 Jia Y, Yang Z, Li H, et al. Reduced graphene oxide encapsulated MnO microspheres as an anode for high-rate lithium ion capacitors. New Carbon Mater, 2021, 36: 573–584
44 Oh S M, Kim I Y, Adpakpang K, et al. The beneficial effect of nanocrystalline and amorphous nature on the anode performance of manganese oxide for lithium ion batteries. Electrochim Acta, 2015, 174: 391–399
45 Wu H, Zhou S, Tseng C, et al. One-pot solution combustion synthesis of crystalline and amorphous molybdenum trioxide as anode for lithium-ion battery. J Am Ceram Soc, 2020, 104: 1102–1109
46 Wu Y, Fee J, Tobin Z, et al. Amorphous manganese oxides: An approach for reversible aqueous zinc-ion batteries. ACS Appl Energy Mater, 2020, 3: 1627–1633
47 Chen M, Liu J, Chao D, et al. Porous α-Fe_2O_3 nanorods supported on carbon nanotubes-graphene foam as superior anode for lithium ion batteries. Nano Energy, 2014, 9: 364–372
48 Jadhav H S, Rai A K, Lee J Y, et al. Enhanced electrochemical performance of flower-like Co_3O_4 as an anode material for high performance lithium-ion batteries. Electrochim Acta, 2014, 146: 270–277
49 Jia B, Chen W, Luo J, et al. Construction of MnO_2 artificial leaf with atomic thickness as highly stable battery anodes. Adv Mater, 2020, 32: 1906582
50 Gogotsi Y, Penner R M. Energy storage in nanomaterials-capacitive, pseudocapacitive, or battery-like? ACS Nano, 2018, 12: 2081–2083
51 Choi C, Ashby D S, Butts D M, et al. Achieving high energy density and high power density with pseudocapacitive materials. Nat Rev Mater, 2020, 5: 5–19
52 Wang X, Liu J, Hu Y, et al. Oxygen vacancy-expedited ion diffusivity in transition-metal oxides for high-performance lithium-ion batteries. Sci China Mater, 2022, 65: 1421–1430
53 Fang G, Wu Z, Zhou J, et al. Observation of pseudocapacitive effect and fast ion diffusion in bimetallic sulfides as an advanced sodium-ion battery anode. Adv Energy Mater, 2018, 8: 1703155
54 Wang Y, Liu H, Wang K, et al. Synthesis and electrochemical performance of nano-sized $Li_4Ti_5O_{12}$ with double surface modification of Ti(III) and carbon. J Mater Chem, 2009, 19: 6789–6795
55 Zhu K, Wang X, Liu J, et al. Novel amorphous MoS_2/MoO_3/nitrogen-doped carbon composite with excellent electrochemical performance for lithium ion batteries Q el batterbon. Ch □, □